

# Examining the Consistency of Precipitation Rate Estimates between the TRMM and GPM Ku-Band Radars

Shinta Seto

Graduate School of Engineering, Nagasaki University, Nagasaki, Japan

## Abstract

For over 20 years, precipitation measurement has continued with spaceborne radars including the Precipitation Radar (PR) operating at 13.8 GHz on the Tropical Rainfall Measuring Mission and the Ku-band Precipitation Radar (KuPR) operating at 13.6 GHz on the Global Precipitation Measurement mission core satellite. PR and KuPR have essentially the same hardware designs and the same algorithm to make standard products (PRV8 and KuPRV06, respectively). The surface precipitation rate estimates ( $R$ ) and related variables are statistically compared between PR and KuPR for a common observation area (within 35°N and 35°S) and period (April to September 2014). Due to the difference in sensitivity, the total precipitation amount recorded by KuPR is larger than recorded by PR by approximately 1.3%. For heavy precipitation, PR shows a smaller measured radar reflectivity factor ( $Z_m$ ) and a larger  $R$  than KuPR.  $Z_m$  is affected by the attenuation and it is smaller for PR than KuPR, as the frequency is slightly higher. The attenuation corrected radar reflectivity factor is almost the same for PR and KuPR. However, the adjustment factor is larger for PR, which results in a larger  $R$ . Direct comparison between PR and KuPR during matchup cases demonstrates similar results.

(Citation: Seto, S., 2022: Examining the consistency of precipitation rate estimates between the TRMM and GPM Ku-band radars. *SOLA*, 18, 53–57, doi:10.2151/sola.2022-009.)

## 1. Introduction

The Precipitation Radar (PR) on the Tropical Rainfall Measuring Mission (TRMM) normally operated from December 1997 to October 2014 (Kanamaru et al. 2017). As a successor, the Dual-frequency Precipitation Radar (DPR) on the Global Precipitation Measurement (GPM) mission core satellite has been operating since March 2014. Precipitation measurement by spaceborne radars has continued for over 20 years (Nakamura 2021). The DPR is composed of a Ku-band Precipitation Radar (KuPR) operating at 13.60 GHz and a Ka-band Precipitation Radar (KaPR) operating at 35.55 GHz, while PR is a Ku-band radar operating at 13.80 GHz. For DPR, three types of standard product are available (KuPR-only product, KaPR-only product, and dual-frequency product), and the latest version as of November 2021 is version 06 (KuPRV06, KaPRV06, and DPRV06 respectively). For the standard PR product, version 7 was the final when the TRMM mission ended. Later, the algorithm for KuPRV06 is applied to PR observations, and a new standard PR product has been published (PR version 8 or PRV8). Long-term analyses of precipitation were conducted by connecting PRV8 and KuPRV06 (e.g. Wang and Tang 2020; Takahashi and Fujinami 2021). The consistency of the two products must be carefully investigated for a more accurate analysis.

PR and KuPR are Ku-band radars and have similar hardware designs. They employ cross-track scanning and measure 49 angle bins per scan, where the zenith angle of angle bin  $j$  ( $1-49$ ) is approximately  $0.7 \times |j - 25|$  degrees. Conversely, there are some

differences as follows.

- PR's frequency is slightly higher than KuPR's frequency by 0.2 GHz.
- The minimum detectable  $Z_m$  is 20.21 dBZ for PR (after the orbit boost), while it is 15.46 dBZ for KuPR (Masaki et al. 2022). KuPR's sensitivity is better than the value expected before the launch (Toyoshima et al. 2015; Hamada and Takayabu 2016).
- KuPR is affected by sidelobe clutter. A method to remove sidelobe clutter was developed by Kubota et al. (2016) and is applied for KuPRV06, but some effects remain at specific angle bins and altitudes. Alternatively, the PR had a beam mismatch issue after the orbit boost. A correction method for the beam mismatch was developed by Kanamaru et al. (2019) and is applied to PRV8, but the decrease of precipitation rate in the latter half of the scan partly remains.

In this study, PRV8 and KuPRV06 are analyzed during a common observation area (within 35°N and 35°S) and period (April to September 2014) to compare the surface precipitation rate estimates and investigate the causes of the differences. The precipitation rate estimation method for KuPRV06 and PRV8 is summarized in Section 2. The surface precipitation rate estimates and related variables are statistically compared between PRV8 and KuPRV06 in Section 3. Direct comparison during matchup cases is presented in Section 4. A summary and conclusions are given in Section 5.

## 2. Precipitation rate estimation method

The precipitation rate estimation method for KuPRV06 is described in Seto et al. (2021). The same method is applied for PRV8. A brief summary of the method is provided here to introduce variables which will be analyzed in the following sections. The major inputs are measured radar reflectivity factor ( $Z_m$ ) and the first guess of path integrated attenuation (PIA) by the surface reference technique (SRT), the latter of which is denoted by PIA<sub>SRT</sub>. The major outputs are the attenuation-corrected radar reflectivity factor ( $Z_e$ ) and precipitation rate ( $R$ ; in mm h<sup>-1</sup>). The relation between  $Z_m$  and  $Z_e$  is shown in Eq. (1).

$$10\log_{10} Z_m(r) = 10\log_{10} Z_e(r) - 2 \int_0^r k(s) ds, \quad (1)$$

where  $r$  is the along-beam distance from the precipitation top (km),  $s$  is a dummy variable of  $r$ , and  $k$  is specific attenuation (dB km<sup>-1</sup>). PIA is calculated using Eq. (2).

$$\text{PIA} = 2 \int_0^{r_s} k(s) ds, \quad (2)$$

where  $r_s$  is the along-beam distance from the precipitation top to the surface.

If the relation in Eq. (3) is assumed,  $Z_e$  and PIA are calculated using Eqs. (4) and (5) (Hitschfeld and Bordan 1954).

$$k(r) = \varepsilon \alpha(r) Z_e(r)^\beta, \quad (3)$$

$$Z_e(r) = Z_m(r) [1 - \varepsilon \zeta(r)]^{-1/\beta}, \quad (4)$$

$$\text{and } \text{PIA} = -\frac{10}{\beta} \log_{10} [1 - \varepsilon \zeta(r_s)], \quad (5)$$

Corresponding author: Shinta Seto, Graduate School of Engineering, Nagasaki University, 1-14 Bunkyo-machi, Nagasaki, Nagasaki 852-8521, Japan. E-mail: seto@nagasaki-u.ac.jp.

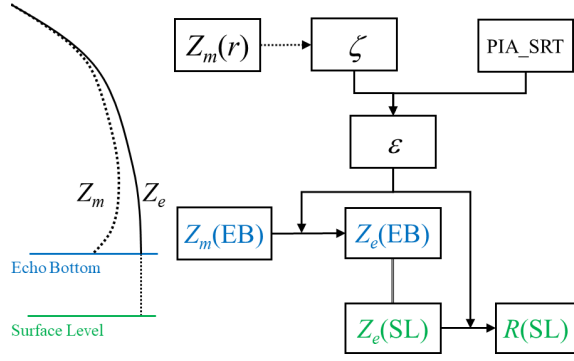


Fig. 1. A flowchart to show the relationship between the key variables for the precipitation rate estimation.

$$\text{where } \zeta(r) \equiv 0.2\beta \ln 10 \int_0^r \alpha(s) Z_m^\beta(s) ds, \quad (6)$$

where  $\beta$  and  $\varepsilon$  are constants, and  $\alpha$  is dependent on  $r$ . This method was adopted in the algorithm for the standard PR product until version 7 (Iguchi et al. 2009). In the algorithm for KuPRV06 and PRV8, Eq. (7) is used instead of Eq. (3), and  $Z_e$  and PIA are numerically calculated.

$$R = \varepsilon^c a D_m^b, \quad (7)$$

where  $D_m$  is mass-weighted mean drop size (mm) and  $a$ ,  $b$  and  $c$  are constants depending on the precipitation type. As both Eqs. (3) and (7) are derived from the same relations between Rayleigh's radar reflectivity factor and  $R$ , which were presented in Kozu et al. (2009), they are equivalent except for approximation error. Therefore, Eqs. (4)–(6) can be used to explain the relationship among the variables in KuPRV06 and PRV8.  $\zeta(r_s)$  is not an output in the standard products, but it is calculated from PIA and  $\varepsilon$  using Eq. (5) with  $\beta = 0.7923$  for stratiform precipitation and  $\beta = 0.7713$  for convective precipitation. Hereafter,  $\zeta(r_s)$  is simply denoted by  $\zeta$ .

$\varepsilon$  is an adjustment factor to explain the variation of drop size distribution and is assumed to follow a log-normal distribution. The PIA\_SRT error is assumed to follow a normal distribution.  $\varepsilon$  is determined to maximize the simultaneous probability of  $\varepsilon$  and PIA\_SRT or to minimize the value of Eq. (8).

$$\left\{ \frac{PIA\_SRT + 10 \log_{10} [1 - \varepsilon \zeta(r_s)] / \beta}{\sigma_{SRT}} \right\}^2 + \left( \frac{\log_{10} \varepsilon - \mu_x}{\sigma_x} \right)^2, \quad (8)$$

where  $\mu_x$  and  $\sigma_x$  are the average and standard deviation of  $\log_{10} \varepsilon$  respectively, and  $\sigma_{SRT}$  is the standard error of PIA\_SRT.

$Z_m$  is not available as a precipitation echo at or near the surface level (SL) because of ground clutter. The lowest height at which  $Z_m$  is available as a precipitation echo is called the echo bottom (EB). Below EB,  $Z_e$  is assumed to be constant along the beam. The key variables used to estimate  $R(SL)$  are  $Z_m(EB)$ ,  $Z_e(EB)$ ,  $Z_e(SL)$ ,  $\zeta$ , PIA\_SRT and  $\varepsilon$  (Fig. 1).  $Z_e(EB)$  is equal to  $Z_e(SL)$ .  $\varepsilon$  affects both the attenuation correction and conversion from  $Z_e$  to  $R$ .

### 3. Statistical comparison

The  $R(SL)$  of PR and KuPR are statistically compared. Hereafter,  $R(SL)$  is simply denoted by  $R$ . Because of the limited number of samples, spatial and temporal variations are not considered.

Firstly, precipitation amount is calculated by dividing the sum of  $R$  by the number of pixels (including  $R = 0$ ) for each angle bin (Fig. 2). It is common that light precipitation is more likely to be missed and the precipitation amount is smaller at angle bins close to 1 or 49 in PR and KuPR, because the mainlobe clutter appears at higher altitude. The precipitation amount has a peak at angle

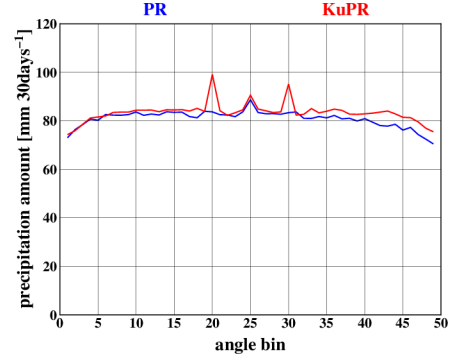


Fig. 2. Precipitation amount (mm 30days<sup>-1</sup>) for each angle bin. The blue line represents PR and the red line represents KuPR.

bin 25 mainly because SRT is unstable at nadir over land (Hirose et al. 2021). At angle bins 20 and 30 of KuPR,  $R$  is unnaturally high due to the sidelobe clutter. In PR,  $R$  is slightly lower at angle bins after 25 than at angle bins before 25 due to beam mismatch. Considering these characteristics, the data at angle bins between 1 and 24 (excluding 20) are used in the analysis of this section.

Next, histograms for  $R$  are produced.  $R$  is converted to dBR ( $10 \log_{10} R$ ) and is categorized as follows. Category 1 is for dBR  $< -10$  ( $R < 0.1$  mm h<sup>-1</sup>), category  $I$  ( $I = 2-35$ ) is for  $(I - 12) \leq \text{dBR} < (I - 11)$ , and category 36 is for  $24 \leq \text{dBR}$  (251 mm h<sup>-1</sup>  $\leq R$ ). In latitude zone  $J$  (1–70) between  $(J - 36)^\circ$  and  $(J - 35)^\circ$ , the number of pixels (including  $R = 0$ ) is denoted as  $N(J)$ . The number of pixels and the average of  $R$  of category  $I$  and in zone  $J$  are denoted as  $n(I, J)$  and  $R_a(I, J)$  respectively. The frequency  $f(I)$  and the precipitation amount  $R_c(I)$  (mm 30days<sup>-1</sup>) over all latitude zones are calculated using Eqs. (9) and (10), respectively.

$$f(I) = \frac{\sum_{J=1}^{70} \frac{n(I, J) w(J)}{N(J)}}{\sum_{J=1}^{70} w(J)} \quad (9)$$

$$\text{and } R_c(I) = \frac{\sum_{J=1}^{70} \frac{n(I, J) R_a(I, J) w(J)}{N(J)}}{\sum_{J=1}^{70} w(J)} \times 720, \quad (10)$$

where  $w(J)$  denotes the area of zone  $J$ .  $\sum_{I=1}^{36} f(I)$  gives the total frequency of precipitation and  $\sum_{I=1}^{36} R_c(I)$  is the total precipitation amount. For KuPR,  $\sum_{I=1}^{36} f(I) = 0.0479$  and  $\sum_{I=1}^{36} R_c(I) = 82.7$ . For PR,  $\sum_{I=1}^{36} f(I) = 0.0356$  and  $\sum_{I=1}^{36} R_c(I) = 81.7$ . These values are smaller than those of KuPR by approximately 26% and 1.3%, respectively.

Figures 3a and 3b show  $f(I)$  and  $R_c(I)$  respectively. Figure 3a clearly shows the difference in sensitivity between PR and KuPR. For PR,  $f(I)$  is almost zero under  $-5$  dBR ( $\sim 0.32$  mm h<sup>-1</sup>). For KuPR,  $f(I)$  is almost zero under  $-9$  dBR ( $\sim 0.13$  mm h<sup>-1</sup>). Causes of the peaks around the minimum detectable level are not clearly understood. Figure 3b reveals the difference in  $R_c(I)$  over 5 dBR ( $\sim 3.2$  mm h<sup>-1</sup>) between PR and KuPR.

The key variables used in the estimation are analyzed to investigate the causes of the difference in  $R$ . For category  $I$ , the average of variable  $X$  is denoted by  $\bar{X}(I)$  and is calculated in Eq. (11).

$$\bar{X}(I) = \frac{\sum_{J=1}^{70} \frac{n(I, J) X(I, J) w(J)}{N(J)}}{\sum_{J=1}^{70} \frac{n(I, J) w(J)}{N(J)}}. \quad (11)$$

For the median of category  $I$ , the exceedance probability  $F(I)$  is calculated in Eq. (12).

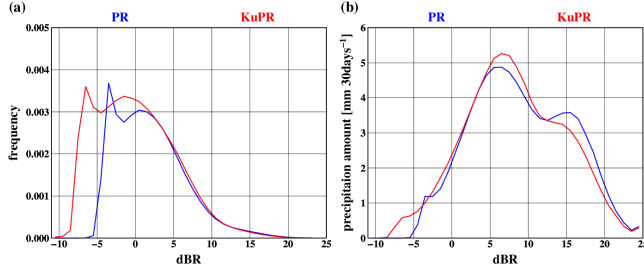


Fig. 3. Histogram of surface precipitation rate estimates. The blue line represents PR and the red line represents KuPR. (a) Frequency is the ratio of the number of pixels to the total number of pixels including  $R = 0$ . (b) Precipitation amount ( $\text{mm } 30\text{days}^{-1}$ ) is the sum of surface precipitation rate estimates divided by the total number of pixels including  $R = 0$ .

$$F(I) = \frac{\sum_{K=1}^{36} \sum_{J=1}^{70} \left(1 - \frac{\delta_{KI}}{2}\right) \frac{n(K, J)w(J)}{N(J)}}{\sum_{J=1}^{70} w(J)}, \quad (12)$$

where  $K$  is a dummy variable of  $I$  and  $\delta_{KI}$  is Kronecker delta.

Samples with the same exceedance probability are compared. In Fig. 4, the horizontal axis is  $F(I)$  and the vertical axis is  $\bar{X}(I)$ . The horizontal axis is on the logarithmic scale to focus on heavy precipitation. As variable  $X$ , (a)  $Z_m(\text{EB})$ , (b)  $\zeta$ , (c) PIA\_SRT, (d)  $\varepsilon$ , (e)  $Z_e(\text{SL})$ , and (f)  $R$  are taken. Under  $-5$  dBR for PR and under  $-9$  dBR for KuPR, the number of samples is very small and the data is not shown.

In Figs. 4a and 4b, for heavy precipitation with the exceedance probability under  $10^{-3}$ , PR shows smaller  $Z_m(\text{EB})$  and  $\zeta$  than KuPR. According to the definition of  $\zeta$  in Eq. (6), a smaller  $\zeta$  suggests that  $Z_m$  is smaller not only at EB, but at other range bins. In Fig. 4c, PR shows a larger PIA\_SRT than KuPR. In Fig. 4d, PR's  $\varepsilon$  is larger than KuPR's excluding where the exceedance probability is under  $10^{-5}$ . At the extreme end, KuPR's  $\varepsilon$  decreases because SRT is sometimes unavailable at extreme precipitation (Seto et al. 2021). PR's  $\varepsilon$  shows a decrease with lower precipitation rates than KuPR's, which may be related to lower sensitivity of PR.

As  $\zeta$  is small and PIA\_SRT is large,  $\varepsilon$  becomes large to minimize the value of Eq. (8). In Fig. 4e, the difference in  $Z_e(\text{SL})$  is almost zero, partly because of the cancelation of the differences in  $Z_m(\text{EB})$  and PIA\_SRT. In Fig. 4f, for heavy precipitation with an exceedance probability under  $10^{-3}$ , PR shows a larger  $R$  than KuPR. It is reasonable that  $R$  increases if  $\varepsilon$  is larger (Seto et al. 2021).

The reasons why  $Z_m$  becomes smaller in PR than in KuPR are discussed here. As the calibration is performed using the same type of device and the same method for PR and KuPR (Masaki et al. 2022), measurement errors should not be the main reason. In Fig. 4a,  $Z_m$  first increases but then decreases after the peak value of approximately 37 dBZ due to the attenuation. While  $Z_m$  increases, no significant difference is observed between PR and KuPR, but the PR value is smaller than that of KuPR, while  $Z_m$  decreases. This strongly suggests that the difference in attenuation causes a difference in  $Z_m$ . The result of PIA\_SRT also suggests that the attenuation is larger for PR.

The effect of frequency difference (13.6 GHz and 13.8 GHz) on the attenuation is calculated according to Mie scattering. The drop size distribution in Eq. (13) is assumed with  $N_w = 10000$ ,  $D_m = 1.5$  mm and  $\mu = 3$ .

$$N(D) = N_w \frac{6(\mu+4)^{\mu+4}}{4^4 \Gamma(\mu+4)} \left(\frac{D}{D_m}\right)^{\mu} \exp\left[-\frac{(\mu+4)D}{D_m}\right]. \quad (13)$$

This exhibits a very heavy precipitation case as the precipitation rate is calculated to be  $109 \text{ mm h}^{-1}$  with a falling velocity  $V = 3.78D^{0.67} \text{ (m s}^{-1}\text{)}$ . According to Mie scattering theory,  $Z_e = 48.15$  dBZ and  $k = 3.43 \text{ dB km}^{-1}$  for 13.60 GHz (KuPR), while  $Z_e =$

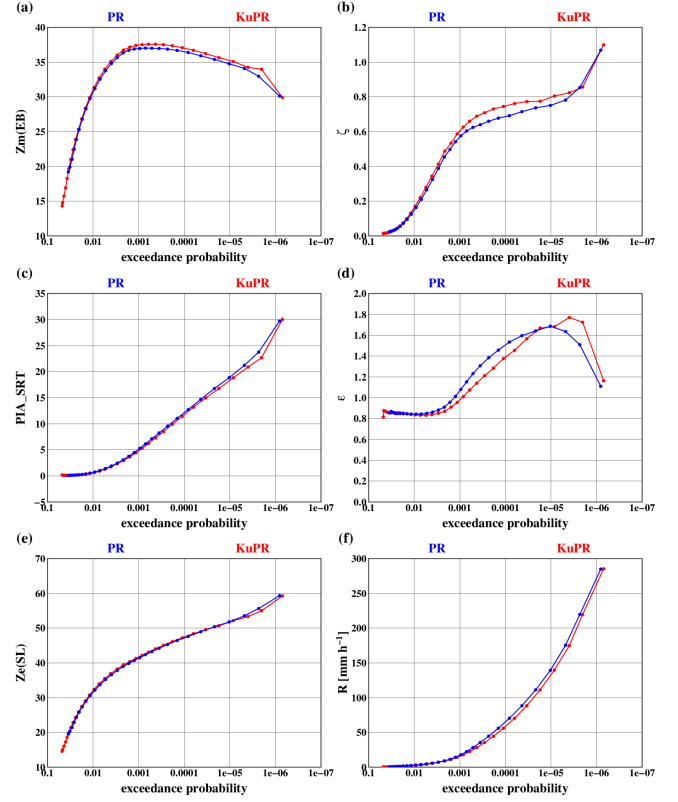


Fig. 4. The relation of the exceedance probability of  $R$  and the average of the variable. The blue line represents PR and the red line represents KuPR. The variable is (a)  $Z_m(\text{EB})$ , (b)  $\zeta$ , (c) PIA\_SRT, (d)  $\varepsilon$ , (e)  $Z_e(\text{SL})$ , (f)  $R$ .

48.18 dBZ and  $k = 3.56 \text{ dB km}^{-1}$  for 13.80 GHz (PR).  $Z_e$  is almost the same but  $k$  shows a difference of approximately 3%. This corresponds to a difference in  $Z_m$  and PIA of approximately 1 dB if the value of PIA is 30 dB. The difference of frequency can be a cause of the difference in  $Z_m$  and PIA\_SRT between PR and KuPR.

#### 4. Comparison at matchup cases

The PRV8 and KuPRV06 are compared in matchup cases where the orbits of the TRMM and GPM core satellite cross each other within 1 minute. The details of the matchup method are described in Supplemental document. Although a total of 125 matchup cases are found in 6 months, the number of cases with precipitation is limited (Fig. S1). In this section, all angle bins 1–49 (excluding 20 and 30) are used as the number of sampling is limited. It should be noted that the beam-mismatch effect and other angle bin dependence of  $R$  may affect the analysis.

A matchup case with TRMM orbit #95909 and GPM core satellite orbit #3138 occurred at 9:29 AM on September 17, 2014 around  $128^\circ\text{E}$ – $131^\circ\text{E}$  and  $11^\circ\text{N}$ – $14^\circ\text{N}$ . Figures 5a and 5b show the  $R$  of PR and KuPR, respectively. Though the two figures are similar, a larger area with  $R > 0$  is seen in KuPR due to the difference in sensitivity. For the matchup pairs, the difference in dBR is shown in Fig. 5c, where heavy precipitation area is focused and 10 pairs are marked as  $R$  is higher than  $50 \text{ mm h}^{-1}$  and precipitation type is convective both for PR and KuPR.

A scatterplot of  $R$  between PR and KuPR is shown in Fig. 6a including all matchup cases. The blue and red dots are used for the 10 pairs shown in Fig. 5c. The purple solid line connects the average of plots in each category separated by purple dotted lines, which show a  $10 \text{ mm h}^{-1}$  step of the average of PR's  $R$  and KuPR's  $R$ . Purple solid line is called the average line and



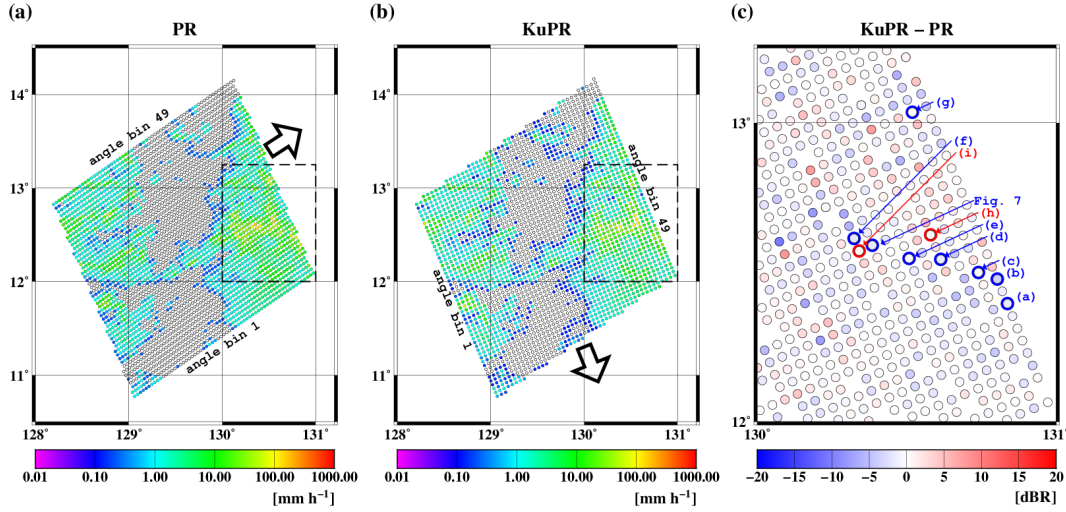


Fig. 5. For the matchup case of TRMM (orbit number 95909) and GPM core satellite (orbit number 3138) around 9:29 AM on 17 September 2014, (a)  $R$  in PR, (b)  $R$  in KuPR, (c) the difference of dBR (KuPR-PR) are shown by colors inside the pixel. (c) show the area which are surrounded by dashed line in (a). In (c), if  $R$  is higher than  $50 \text{ mm h}^{-1}$  and precipitation type is convective both for PR and KuPR, pixels are surrounded by bold circles; blue (red) circle means  $R$  in PR is higher (lower) than  $R$  in KuPR.

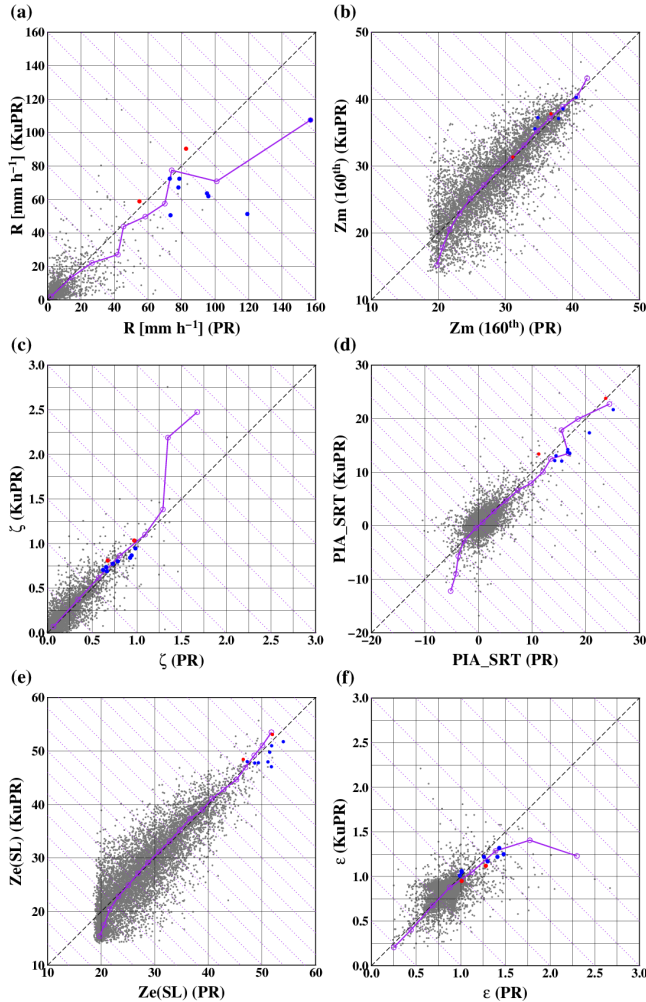


Fig. 6. Scatterplots of the variables between PR and KuPR. The blue (red) dots correspond to the pixels surrounded by blue (red) circles in Fig. 5c. The variable is (a)  $R$ , (b)  $Z_m$  at the  $160^{\text{th}}$  range bin, (c)  $\zeta$ , (d)  $\text{PIA\_SRT}$ , (e)  $Z_e(\text{SL})$ , (f)  $\varepsilon$ .

is drawn in similar way in Figs. 6b–6f. As the average line is lower than 1-by-1 line in Fig. 6a,  $R$  tends to be larger for PR than KuPR. Figure 6b shows the scatterplot of  $Z_m$  at the  $160^{\text{th}}$  range bin (approximately 2 km in height from the Ellipsoid). As the EB changed by angle bin numbers,  $Z_m(160^{\text{th}})$  is used instead of  $Z_m(\text{EB})$ . If  $Z_m(160^{\text{th}})$  is not available as a precipitation echo for PR and/or KuPR, the pair is not plotted. The average line is slightly higher than 1-by-1 line. Figures 6c–f show the scatterplot of  $\zeta$ ,  $\text{PIA\_SRT}$ ,  $\varepsilon$ , and  $Z_e(\text{SL})$ , respectively. According to the location of the average line against 1-by-1 line,  $\text{PIA\_SRT}$  and  $\varepsilon$  tend to be larger for PR, while  $\zeta$  tends to be larger for KuPR.  $Z_e(\text{SL})$  of PR is closer to that of KuPR. These results are agreed with the results shown in Section 3.

Figure 7 shows the vertical profile of  $Z_m$ ,  $Z_e$ , and  $R$  at the pixel (as marked in Fig. 5c), where  $R$  is  $157 \text{ mm h}^{-1}$  for PR (angle bin 17) and  $107 \text{ mm h}^{-1}$  for KuPR (angle bin 42). The EB is lower for PR as the zenith angle is smaller. On the other hand, KuPR's  $Z_m$  is available up to higher altitude due to its better sensitivity. Except for these differences, the profiles of  $Z_m$  agreed well with each other, but PR's  $Z_m$  shows a larger decrease in going downwards than KuPR's, which may be partly caused by the difference in attenuation. At lower range bins,  $Z_m$  is smaller for PR, but  $Z_e$  and  $R$  are larger for PR. It is not only because of  $\varepsilon$  (1.26 for PR and 1.22 for KuPR), but because of  $\text{PIA\_SRT}$  (25.1 dB for PR and 21.2 dB for KuPR). The vertical profiles of  $Z_m$ ,  $Z_e$ , and  $R$  for the other nine pixels are shown in Fig. S2. At some pixels, larger decrease in  $Z_m$  is seen for PR.

## 5. Summary and conclusions

Precipitation rate estimates of PRV8 and KuPRV06 are compared and the reasons for the differences are investigated. In both the statistical comparison (Section 3) and the direct comparison at matchup cases (Section 4),  $R$  tends to be larger for PR for heavy precipitation cases. This can be partly caused by the difference of attenuation between 13.6 GHz and 13.8 GHz. In PR,  $Z_m$  is smaller and  $\text{PIA\_SRT}$  is larger, resulting in larger  $\varepsilon$  and  $R$ .

Among the differences between PR and KuPR listed in Section 1, the difference of frequency affects heavy precipitation estimates. The difference in sensitivity affects the total precipitation frequency and amount. The effects of sidelobe clutter and beam mismatch remain at some angle bins. For the analysis of a long-term dataset connecting PR and KuPR, it is worth noting that the precipitation amount calculated for all data is affected by the

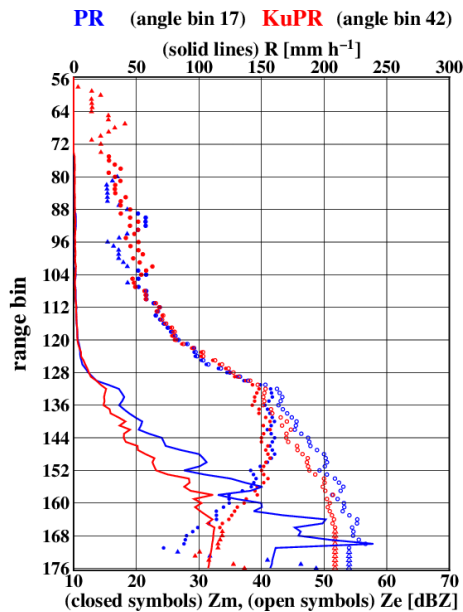


Fig. 7. The vertical profile of  $Z_m$ ,  $Z_e$ , and  $R$  at the pixel (angle bin 17 for PR and 42 for KuPR; shown in Fig. 5c). The blue symbols represent PR and the red symbols represent KuPR. The closed circles represent  $Z_m$  which is used as the precipitation echo. The closed triangles represent  $Z_m$  which is not used as the precipitation echo. Open circles and triangles represent  $Z_e$  corresponding to open symbols  $Z_m$ . Solid lines represent the precipitation rate estimates. The vertical axis shows the range bin number (each range bin has the width of 125 m).

difference of sensitivity. Calculation of the precipitation amount for samples with the same exceedance probability is an alternative idea. The effects of frequency difference on attenuation should be considered in future algorithm updates.

## Acknowledgements

This work was financially supported by JAXA under Research Announcement on the Earth Observations. The author is grateful to the DPR Level-2 algorithm team members for their kind advice.

Edited by: T. Nasuno

## Supplements

Supplemental Document describes the procedure to matchup PR and KuPR data. Supplemental Figures include two figures; Fig. S1 shows the area where a matchup of PR and KuPR occurred and Fig. S2 shows the vertical profiles of  $Z_m$ ,  $Z_e$ , and  $R$  at heavy precipitation pixels.

## References

- Hamada, A., and Y. N. Takayabu, 2016: Improvements in detection of light precipitation with the Global Precipitation Measurement Dual-frequency Precipitation Radar (GPM/DPR). *J. Atmos. Oceanic Technol.*, **33**, 653–667.
- Hirose, M., S. Shige, T. Kubota, F. A. Furuzawa, H. Minda, and H. Masunaga, 2021: Refinement of surface precipitation estimates for the Dual-frequency Precipitation Radar on the GPM Core Observatory using near-nadir measurements. *J. Meteor. Soc. Japan*, **99**, 1231–1252.
- Hitschfeld, W., and J. Bordan, 1954: Errors inherent in the radar measurements of rainfall at attenuating wavelength. *J. Atmos. Sci.*, **11**, 58–67.
- Iguchi, T., T. Kozu, J. Kwiatkowski, R. Meneghini, J. Awaka, and K. Okamoto, 2009: Uncertainties in the rain profiling algorithm for the TRMM Precipitation Radar. *J. Meteor. Soc. Japan*, **87A**, 1–30.
- Kanamaru, K., T. Kubota, T. Iguchi, Y. N. Takayabu, and R. Oki, 2017: Development of a precipitation climate record from spaceborne precipitation radar data. Part I: Mitigation of the effects of switching to redundancy electronics in the TRMM Precipitation Radar. *J. Atmos. Ocean Technol.*, **34**, 2043–2057.
- Kanamaru, K., T. Kubota, and T. Iguchi, 2019: Improvements in the beam-mismatch correction of Precipitation Radar data after the TRMM orbit boost. *IEEE Trans. Geosci. Remote Sens.*, **57**, 7161–7169.
- Kozu, T., T. Iguchi, T. Kubota, N. Yoshida, S. Seto, J. Kwiatkowski, and Y. N. Takayabu, 2009: Feasibility of raindrop size distribution parameter estimation with TRMM Precipitation Radar rain retrieval algorithm. *J. Appl. Meteor. Climatol.*, **48**, 716–724.
- Kubota, T., T. Iguchi, M. Kojima, L. Liao, T. Masaki, H. Hanado, R. Meneghini, and R. Oki, 2016: A statistical method for the reducing sidelobe clutter for the Ku-band Precipitation Radar on board the GPM core observatory. *J. Atmos. Ocean. Technol.*, **33**, 1413–1428.
- Masaki, T., T. Iguchi, K. Kanamaru, K. Furukawa, N. Yoshida, T. Kubota, and R. Oki, 2022: Calibration of the Dual-frequency Precipitation Radar (DPR) onboard the Global Precipitation Measurement (GPM) core observatory. *IEEE Trans. Geosci. Remote Sens.*, doi:10.1109/TGRS.2020.3039978.
- Nakamura, K., 2021: Progress from TRMM to GPM. *J. Meteor. Soc. Japan*, **99**, 697–729.
- Seto, S., T. Iguchi, R. Meneghini, J. Awaka, T. Kubota, T. Masaki, and N. Takahashi, 2021: The precipitation rate retrieval algorithms for the GPM Dual-frequency Precipitation Radar. *J. Meteor. Soc. Japan*, **99**, 205–237.
- Takahashi, H. G., and H. Fujinami, 2021: Recent decadal enhancement of Meiyu-Baiu heavy rainfall over East Asia. *Sci. Rep.*, **11**, 13665, doi:10.1038/s41598-021-93006-0.
- Toyoshima, K., H. Masunaga, and F. A. Furuzawa, 2015: Early evaluation of Ku- and Ka-band sensitivities for the Global Precipitation Measurement (GPM) Dual-frequency Precipitation Radar (DPR). *SOLA*, **11**, 14–17.
- Wang, T., and G. Tang, 2020: Spatial variability and linkage between extreme convections and extreme precipitation revealed by 22-year space-borne precipitation radar data. *Geophys. Res. Lett.*, **47**, 1–10, doi:10.1029/2020GL088437.

Manuscript received 19 November 2021, accepted 20 January 2022  
SOLA: <https://www.jstage.jst.go.jp/browse/sola/>